NeuroImage: Clinical 22 (2019) 101741

Contents lists available at ScienceDirect

NeuroImage: Clinical

journal homepage: www.elsevier.com/locate/ynicl

Physiological significance of R-fMRI indices: Can functional metrics differentiate structural lesions (brain tumors)?

Zhen Fan[a,1], Xiao Chen[b,c,1], Zeng-Xin Qi[a], Le Li[b,d], Bin Lu[b,c], Cong-Lin Jiang[a], Ren-Qing Zhu[a], Chao-Gan Yan[b,c,d,e,*], Liang Chen[a,**]

[a] Department of Neurosurgery, Huashan Hospital, Fudan University, Shanghai Neurosurgical Clinical Center, Shanghai, China
[b] CAS Key Laboratory of Behavioral Science, Institute of Psychology, Beijing, China
[c] Department of Psychology, University of Chinese Academy of Sciences, Beijing, China
[d] Magnetic Resonance Imaging Research Center, Institute of Psychology, Chinese Academy of Sciences, Beijing, China
[e] Department of Child and Adolescent Psychiatry, NYU Langone Medical Center School of Medicine, New York, NY, USA

ARTICLE INFO

Keywords:
Resting-state fMRI
Standardization
Biomarker
Cerebellum
Tumor

ABSTRACT

Resting-state functional MRI (R-fMRI) research has recently entered the era of "big data", however, few studies have provided a rigorous validation of the physiological underpinnings of R-fMRI indices. Although studies have reported that various neuropsychiatric disorders exhibit abnormalities in R-fMRI measures, these "biomarkers" have not been validated in differentiating structural lesions (brain tumors) as a concept proof. We enrolled 60 patients with intracranial tumors located in the unilateral cranial cavity and 60 matched normal controls to test whether R-fMRI indices can differentiate tumors, which represents a prerequisite for adapting such indices as biomarkers for neuropsychiatric disorders. Common R-fMRI indices of tumors and their counterpart control regions, which were defined as the contralateral normal areas (for amplitude of low frequency fluctuations (ALFF), fractional ALFF (fALFF), regional homogeneity (ReHo) and degree centrality (DC)) and ipsilateral regions surrounding the tumors (for voxel-mirrored homotopic connectivity (VMHC)), were comprehensively assessed. According to robust paired *t*-tests with a Bonferroni correction, only VMHC (Fisher's r-to-z transformed) could successfully differentiate substantial tumors from their counterpart normal regions in patients. Furthermore, ALFF and DC were not able to differentiate tumor from normal unless *Z*-standardization was employed. To validate the lower power of the between-subject design compared to the within-subject design, each metric was calculated in a matched control group, and robust two-sample *t*-tests were used to compare the patient tumors and the normal controls at the same place. Similarly, only VMHC succeeded in differentiating significant differences between tumors and the sham tumor areas of normal controls. This study tested the premise of R-fMRI biomarkers for differentiating lesions, and brings a new understanding to physical significance of the *Z*-standardization.

1. Introduction

Resting-state functional magnetic resonance imaging (R-fMRI) is one of the most rapidly expanding areas of neuroimaging research. As ease of data collection in diseased people, and amenability to aggregation across studies and sites, R-fMRI is particularly suitable for clinical applications (Biswal et al., 2010; Castellanos et al., 2013; Yan et al., 2013b; Zuo and Xing, 2014). An increasing number of R-fMRI indices have been proposed to characterize clinical populations with various neuropsychiatric disorders (Craddock et al., 2013; Zuo and Xing, 2014), and several of these indices have produced consistent and reliable results corresponding to functional areas within single individuals (Castellanos et al., 2013; Lang et al., 2014). As we have entered an era of "Big Data", vast opportunities in R-fMRI research are available to take advantage of advanced data-intensive machine learning methodologies, such as deep learning along with open source computational platforms, to discover validated biomarkers not only for diagnosis but also for assessing disease risk, prognosis and treatment

* Correspondence to: C.G. Yan, CAS Key Laboratory of Behavioral Science, Institute of Psychology, 16 Lincui Road, Chaoyang District, Beijing 100101, China.
** Correspondence to: L. Chen, No. 12 Mid Wulumuqi Rd, Department of Neurosurgery, Hua Shan Hospital, Fudan University, Shanghai Neurosurgery Clinical Center, Shanghai 200040, China.
E-mail addresses: ycg.yan@gmail.com (C.-G. Yan), chenlianghs@126.com (L. Chen).
[1] Zhen Fan and Xiao Chen contributed equally to this work.

https://doi.org/10.1016/j.nicl.2019.101741
Received 2 July 2018; Received in revised form 16 February 2019; Accepted 28 February 2019
Available online 01 March 2019

response (Bzdok and Yeo, 2017; Kapur et al., 2012; Xia and He, 2017). In particular, several promising R-fMRI biomarker studies have recently been reported (Abraham et al., 2017; Drysdale et al., 2017).

However, the physiological mechanisms underlying R-fMRI indices are still not well understood (Liu, 2013; Zhang and Raichle, 2010), although some evidences have been provided in the literature. First, the patterns of the networks defined by R-fMRI spontaneous fluctuations reflect the underlying organizational rules of the brain's anatomy (Baria et al., 2011). This fact was further validated by tract-tracing methods in the non-human primates (Kelly et al., 2010; Margulies et al., 2009). Second, a series of electrophysiological studies of the brains of humans, non-human primates and other mammalians, particularly those employing intracranial electrodes, linked neural activity to ongoing fMRI fluctuations (Hacker et al., 2017; He et al., 2008; Keller et al., 2011; Leopold and Maier, 2012; Liu et al., 2011; Scholvinck et al., 2013). Moreover, individual differences in behavior and pathology have suggested the validity of assessing R-fMRI fluctuations (Caulfield et al., 2016; Craddock et al., 2013; Di Martino et al., 2014; Nostro et al., 2018). However, all this evidence only partially explains the underpinnings of R-fMRI signals; the details remain unresolved, causing difficulty in interpreting changes in resting-state activity and impeding the path of R-fMRI toward clinical applications (Power et al., 2014).

Prior to further exploring the clinical value of R-fMRI indices, the presuppositions of whether common indices are able to differentiate obvious structural lesions (such as brain tumors) should be considered first. To date, most R-fMRI studies of brain tumors have focused on surgical planning to identify and locate the eloquent areas in order to reduce the risk of postoperative functional deficits (Lang et al., 2014; Pernet et al., 2016; Qiu et al., 2014; Zhang and Raichle, 2010). However, few studies have systematically explored the signals of tumors themselves as a proof-of-concept for utilizing R-fMRI indices in clinical applications. If an R-fMRI index cannot even differentiate obvious structural lesions, it is likely unable to be trusted as a tool for studying diseases without structural lesions or, consequently, as a biomarker for further big data studies. Thus, whether R-fMRI methodologies have the capacity for distinguishing pathological lesions from normal brain structures should be a fundamental prerequisite for further biomarker investigations.

To address these issues, we first comprehensively assessed common R-fMRI metrics of tumors and their counterpart control brain regions, which were defined as contralateral control areas to the tumors (for amplitude of low frequency fluctuations (ALFF), fractional ALFF (fALFF), regional homogeneity (ReHo) and degree centrality (DC)) and ipsilateral regions surrounding the tumors (for voxel-mirrored homotopic connectivity (VMHC)). We used paired *t*-tests to compare each measure between the tumor regions and the counterpart control regions, respectively. Second, to validate the lower power in the between-subject design than in the within-subject design, each metric was calculated in a matched control group, and two-sample *t*-tests were used to compare the patient tumor areas with the same areas in the normal controls. Note that the robust statistical tests were conducted in the present research to control any potential artifacts from outliers. Furthermore, we compared the measures with and without *Z*-standardization (subtracting the brain mean and dividing by the brain standard deviation (SD)) to test the significance of this statistical transformation (Yan et al., 2013b). We hypothesized that (i) R-fMRI metrics can differentiate structural lesions (brain tumors), (ii) Z-standardization can enhance the validity of R-fMRI metrics, and that (iii) within-subject designs are superior to between-subject designs in differentiating tumors.

2. Materials and methods

2.1. Subjects

A total of 60 patients (37 females; 21–72 years) with intracranial tumors were enrolled in this study. The criteria of enrollment were: a) tumor located in the lateral posterior cranial fossa without spreading across the median to the contralateral side, b) without obvious edema, c) not rich vascular masses, such as artery venous malformation (AVM), dural arteriovenous fistula (DAVF) and substantive hemangioblastoma. Meanwhile, 60 sex-matched and age-matched healthy individuals were included as the control group. Approval of this study was provided by the independent Ethics Committee of Huashan Hospital, Fudan University. Written informed consent was obtained from all subjects. All the maps of the R-fMRI indices of this study are shared through the R-fMRI Maps Project (ftp://ftpdownload:FTPDownload@lab.rfmri.org/sharing/RfMRIMaps/PaperDataSharing/Fan_2019_R-fMRIIndices_CerebellarTumor/Fan_2019_R-fMRIIndices_CerebellarTumor.zip).

2.2. Imaging acquisition

All images were acquired using a Siemens Magnetom Verio 3.0 T MRI scanner (Siemens Medical Solutions, MAGNETOM, Germany). All patients were scanned preoperatively using R-fMRI (TR = 2000 ms; TE = 35 ms; flip angle = 90°; slice number = 33; field of view [FOV] = 210 × 210 mm; voxel size = 3.3 × 3.3 × 4.0 mm^3). During the scanning, subjects were asked to remain still with their eyes closed. Soft foam pad was used for fixation and no task was given to the subjects, but they were told not to fall asleep. Scans lasted for 8 min for a total of 240 time points per subject. Each run was preceded by 6-s dummy scans for magnetization stabilization. Additionally, high-resolution anatomical images were acquired with an axial magnetization-prepared rapid gradient echo T1-weighted sequence with contrasts (Gadopentetate Dimeglumine) (TR = 1900 ms; TE = 2.93 ms; flip angle = 90°; matrix size = 256 × 215; number of slices = 176; slice thickness = 1 mm; FOV = 250 × 219 mm).

2.3. Preprocessing

All preprocessing was performed using the Data Processing Assistant for Resting-State fMRI (DPARSF, Yan and Zang, 2010, http://rfmri.org/DPARSF), which is based on Statistical Parametric Mapping (SPM, http://www.fil.ion.ucl.ac.uk/spm) and the toolbox for Data Processing & Analysis of Brain Imaging (DPABI, Yan et al., 2016, http://rfmri.org/DPABI). First, the initial 10 volumes were discarded, and slice-timing correction was performed with all volume slices corrected for different signal acquisition times by shifting the signal measured in each slice relative to the acquisition of the slice at the midpoint of each TR. Then, the time series of images for each subject were realigned using a six-parameter (rigid body) linear transformation with a two-pass procedure (registered to the first image and then registered to the mean of the images after the first realignment). After realignment, individual T1-weighted MPRAGE images were co-registered to the mean functional image using a 6°-of-freedom linear transformation without re-sampling and then segmented into gray matter (GM), white matter (WM) and cerebrospinal fluid (CSF) (Ashburner and Friston, 2005). Finally, transformations from the individual native space to the Montreal Neurological Institute (MNI) space were computed with the Diffeomorphic Anatomical Registration Through Exponentiated Lie algebra (DARTEL) tool (Ashburner, 2007).

2.4. Nuisance regression

To minimize head motion confounds, we utilized the Friston 24-parameter model (Friston et al., 1996) to regress out head motion effects. The Friston 24-parameter model (which considers 6 head motion parameters, the 6 head motion parameters at the previous time point, and the 12 corresponding squared items) was chosen based on prior work indicating that higher-order models remove head motion effects better (Satterthwaite et al., 2013; Yan et al., 2013a). As global signal regression (GSR) is still a controversial practice in the R-fMRI field

(Murphy and Fox, 2016), we examined the results without GSR but performed a validation with GSR in the supplementary analyses. Other sources of spurious variance (WM and CSF signals) were also removed from the data through linear regression to reduce respiratory and cardiac effects. Additionally, linear trends were included as a regressor to account for drifts in the blood oxygen level-dependent (BOLD) signal. We performed temporal bandpass filtering (0.01–0.1 Hz) on all time-series except for ALFF and fALFF analyses.

2.5. A broad array of R-fMRI metrics

Amplitude of low frequency fluctuations (ALFF) (Zang et al., 2007) and fractional ALFF (fALFF) (Zou et al., 2008): ALFF is the mean of amplitudes within a specific frequency domain (here, 0.01–0.1 Hz) from a fast Fourier transform of a voxel's time course. fALFF is a normalized version of ALFF and represents the relative contribution of specific oscillations to the whole detectable frequency range.

Regional homogeneity (ReHo) (Zang et al., 2004): ReHo is a rank-based Kendall's coefficient of concordance (KCC) that assesses the synchronization among a given voxel and its nearest neighbors' (here, 26 voxels) time courses.

Degree centrality (DC) (Buckner et al., 2009; Zuo et al., 2012): DC is the number or sum of weights of significant connections for a voxel. Here, we calculated the weighted sum of positive correlations by requiring each connection's correlation coefficient to exceed a threshold of $r > 0.25$ (Buckner et al., 2009).

Voxel-mirrored homotopic connectivity (Anderson et al., 2011; Zuo et al., 2010b): VMHC corresponds to the functional connectivity between any pairs of symmetric inter-hemispheric voxels, that is, the Pearson's correlation coefficient between the time series of each voxel and that of its counterpart voxel at the same location in the opposite hemisphere. The resultant VMHC values were Fisher-Z transformed. For better correspondence between symmetric voxels, VMHC required that individual functional data be further registered to a symmetric template and smoothed (4 mm FWHM). The group-averaged symmetric template was created by first computing a mean normalized T1 image across participants, and then this image was averaged with its left-right mirrored version (Zuo et al., 2010b).

For further analyses, all of the metric maps were calculated with and without *Z*-standardization (subtracting the mean value for the entire brain from each voxel, and dividing by the corresponding SD) and then smoothed (4 mm FWHM), except for VMHC (which was smoothed beforehand and Fisher's r-to-z transformed).

2.6. Strategies to compare the indices of tumor regions with corresponding control areas

We manually drew the tumor's edge of each subject as the tumor masks using MRIcroN (http://people.cas.sc.edu/rorden/mricron/main.html). Tumors' boundaries were defined by the average of 2 experienced neurosurgeons' advices, which referred to our previous work (Qiu et al., 2014). We determined the boundaries according to the high-resolution T1 images normalized to the MNI spaces using DPABI. One pilocytic astrocytoma and all cholesteatomas' T1 images manifested no enhancement, then we defined their boundaries using high-resolution T1 images without contrast, and others using enhancing images. For ALFF, fALFF, ReHo and DC, corresponding control areas were defined as the normal symmetric inter-hemispheric voxels of the tumors. For VMHC, corresponding control areas were defined at the tumors' periphery, which were derived by enlarging the tumors by 4 voxels and subtracting the original tumor areas, using a MATLAB-based script called y_MaskEnlarge (http://d.rnet.co/Programs_YAN/y_MaskEnlarge.m).

Each metric of the tumor mask and the corresponding control area was then averaged within the mask or the corresponding control area for the same subject, allowing us to perform group-level robust paired *t*-tests for the within-subject design.

To prove that a significant difference did not exist in the null conditions, 60 matched normal controls underwent the same analysis, considering the normal controls to have sham tumors at the same locations as the tumors in the patients, and comparing the five indices of the sham tumors with those of the corresponding sham control regions.

Moreover, to confirm the validity of the within-subject design, we compared each metric of the tumors in the patients with the sham tumors in the matched controls using robust two-sample *t*-tests, as the metrics in this method were derived from different subjects. This procedure allowed us to investigate differences between the within-subject design and the between-subject design.

Given recent concerns about the presentation of neuroimaging data, especially the traditional bar and line graphs (Rousselet et al., 2016; Weissgerber et al., 2015), we chose to use violin graphs to present our main findings. Violin plot is a much more informative and robust graph that can show the full distribution of the data (Rousselet et al., 2016). Multiple comparison is a serious issue, especially in neuroimaging area (Chen et al., 2018; Eklund et al., 2016), we chose the most rigid strategy, namely Bonferroni correction. As we performed 9 *t*-tests for repeated measurements, the significance level was decided to be 0.0056 (0.05/9). Moreover, it should also be noted that Student's *t*-test is based on some assumptions and violations of these assumptions can cause a serious detrimental effect on the mathematical properties of this test (Pernet et al., 2012; Wilcox and Rousselet, 2018). Thus, we used the robust *t*-test which can control the classical Student's *t*-test's oversensitivity to outliers to see whether our findings were driven by violations of statistical assumptions. The robust t-test was conducted based on the in-house MATLAB function “robustfit” which is developed for robust regression. Robust regression (“robustfit” function) specifies a weighted function with a tuning constant. The default tuning constant give coefficient estimate that is approximately 95% as statistically efficient as the ordinary least-squares estimates, provided the response has a normal distribution with no outlier (Dumouchel and O'Brien, 1992). Similar to Student's t-test in the simple general linear model, we constructed a matrix that contains a vector specifying sample pairs and a number of covariates controlling subjects' effects for robust pair t-test. In the robust two sample t-test, only the group vector will be specified.

3. Results

3.1. Overlaps of tumor masks

A total of 60 intracranial tumors located in the unilateral posterior cranial fossa were identified, including 23 tumors located on the left side and 37 tumors on the right side. The pathological outcomes of these tumors were verified after operations and turned out to be the meningioma ($n = 17$), neurinoma ($n = 31$), hemangioblastoma ($n = 5$), pilocytic astrocytoma (n = 3) and cholesteatoma ($n = 4$). Of note, none of these tumors exhibited any neural activity whatsoever, and their original tissues did not contain any neurons. In addition, the edges of these tumors were clear, making them suitable for validating the physiological meaning underlying R-fMRI (Jiang et al., 2010). The tumors overlap probabilistic images are depicted in Fig. 1.

3.2. Comparison between indices of tumor and corresponding control areas in the patient group

We first compared the means of each metric of the tumors and the corresponding control areas in patients. For ALFF, fALFF, ReHo and DC, the corresponding control areas were defined as the tumors' symmetric inter-hemispheric voxels for VMHC, the corresponding control areas were defined as the 4 voxels of the tumors periphery. Robust paired Student's *t*-tests were conducted to determine whether significant differences existed. Without *Z*-standardization, all four indices (ALFF, fALFF, ReHo and DC) failed (cannot survive Bonferroni correction) to

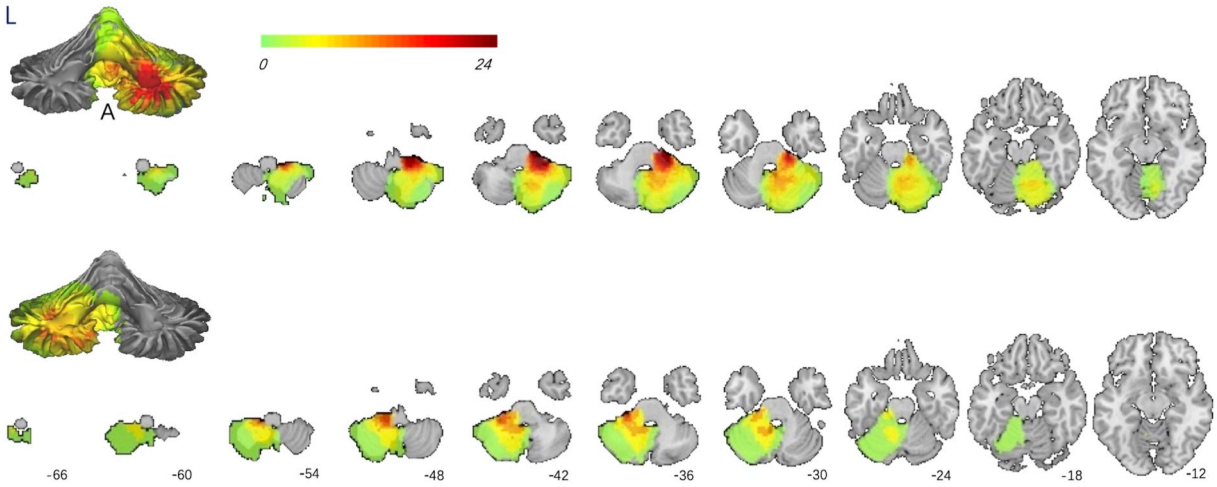

Fig. 1. Overlaps of tumors. A total of 60 patients with intracranial tumors located in unilateral posterior cranial fossa, including 23 tumors located on the left side and 37 tumors located on the right side. The tumors overlap probabilistic figures are shown. The stereo cerebellum is presented in the anterior view, and two-dimensional maps are presented in the transverse view.

distinguish tumors from the corresponding control areas (ALFF $p = .007$, $t_{(60)} = -2.53$; fALFF $p = .009$, $t_{(60)} = -2.44$; ReHo, $p = .067$, $t_{(60)} = -1.516$; DC, $p = .074$, $t_{(60)} = -0.1.47$) (Table 1 and Fig. 2). With *Z*-standardization, ALFF and DC were significantly differed between tumors and the corresponding control areas (ALFF $p = .001$, $t_{(60)} = -3.22$, *Cohen'd* = 0.416; DC, $p < .0001$, $t = -4.20$, *Cohen'd* = 0.542), indicating the ability of its value to distinguish tumors from corresponding control areas. Among 60 patients, 42 and 52 subjects showed the same direction as the group difference, separately. However, fALFF and ReHo failed again in differentiating tumors as their *p* values cannot survive correction (fALFF $p = .008$, $t_{(60)} = -2.51$; ReHo, $p = .030$, $t_{(60)} = -1.91$). In contrast to the above 4 indices, VMHC was Fisher's r-to-z transformed (rather than Z-standardized) and compared with the surrounding control areas (rather than with inter-hemispheric areas). VMHC successfully differentiated tumors ($p < .0001$, $t_{(60)} = -8.869$, *Cohen'd* = 1.121). And 52 out of 60 patients showed the same direction as the group effect.

3.3. Comparison between indices of sham tumors and the corresponding sham control areas in the normal control group

To verify that the significant differences are not false positives (i.e., they do not exist in null conditions), we next compared the five indices of healthy controls' sham tumors with those of the corresponding sham control areas. Not surprisingly, all five indices were not significantly different between the sham tumors and the corresponding sham control areas even without correction ($p > .05$, $n = 60$) regardless of whether *Z*-standardization (not including VMHC) was employed (Table 1 and Fig. 2). This result provided initial validation for the similarities in functions and structures between the tumor areas and the corresponding control regions in these large scales (tumors) analysis, which suggests that the significant results described above for the patient group may not due to false positives.

3.4. Different profiles of R-fMRI indices in differentiating tumors

After employing *Z*-standardization, DC and ALFF along with VMHC were able to differentiate tumors (Fig. 2). To explore the different profiles of the five R-fMRI indices in differentiating tumors, we converted the *p* values to *z* values to identify the differences between tumors and control areas (Fig. 3). VMHC showed the greatest significant difference, followed by DC and ALFF, successively. fALFF and ReHo did not demonstrate significant difference ($p > .0056$). In contrast, the *p* values of the five indices for the controls were all higher than 0.05 regardless of whether Z-standardization (not including VMHC) was employed.

3.5. Between-subject design decreased the power in differentiating tumors

To compare the power of the between-subject design with the within-subject design, we compared each metric of the tumors in the patient group with the metric of sham tumors in the matched control group using robust two samples *t*-tests, as different subjects were being compared. Before employing Z-standardization, ALFF, fALFF, ReHo and DC all failed to distinguish tumors from normal areas (Table 1). Even after employing Z-standardization in this between-subject design, all four indices (ALFF, fALFF, ReHo and DC) failed (cannot survive Bonferroni correction) to distinguish tumors from the corresponding control areas (ALFF, $p = .012$, $t_{(120)} = -2.32$; fALFF, $p = .020$, $t_{(120)} = -2.07$; ReHo, $p = .073$, $t_{(120)} = 1.47$ and DC, $p = .600$, $t_{(120)} = -0.26$)). With Fisher's r-to-z transformation, VMHC ($p = 9.8688 \times 10^{-8}$, $t_{(120)} = -5.6797$, *Cohen'd* = 1.037) again successfully differentiated tumors according to robust unpaired *t*-tests and 53 out of 60 patients showed the same direction as the group difference (Fig. 4).

4. Discussion

The aim of this study was to test the ability of R-fMRI indices to differentiate brain tissues from those without neural signals (brain tumors), which represents a prerequisite for adapting such indices as biomarkers for neuropsychiatric disorders. Note that all of our subjects' tumors do not contain any neurons and no neural activity is supposed to be detected in these tumors. However, as a concept proof, we calculated the "neural activity" indexed by the R-fMRI metrics in these tumors, to see if they were significantly different from those normal areas with real neural activity. If an R-fMRI metric cannot differentiate the tumors from control areas, then it fails the test. Here, we comprehensively assessed five common indices of R-fMRI indices, and we compared the results regarding whether *Z*-standardization was employed or not, except for VMHC, which was Fisher's r-to-z transformed. Interestingly, only ALFF and DC were not able to differentiate tumors from normal neural regions (paired *t*-test, survived Bonferroni correction threshold $p < .05/9 = 0.0056$) unless Z-standardization was performed. These corresponding regions did not show significant differences even without correction when compared with the normal controls (paired *t*-tests, $p > .05$). To verify whether our primary analyses without GSR could be generalized to with GSR, we calculated the results with GSR

Table 1
Statistical results and significance levels of common R-fMRI indices calculated within and between patients and normal controls.

	Robust paired *t*-test within patient group						Robust paired *t*-test within normal controls		
	Without *Z*-Standardization			With *Z*-Standardization			Without *Z*-Standardization		
	t	*p*	*ES*	*t*	*p*	*ES*	*t*	*p*	*ES*
ALFF	−2.5350	0.0070*	0.3273	−3.2237	0.0010**	0.4162	0.6788	0.7500	0.0876
fALFF	−2.4356	0.0090*	0.3144	−2.5068	0.0075*	0.3236	0.8276	0.7944	0.1068
ReHo	−1.5163	0.0674	0.1958	−1.9127	0.0303*	0.2469	−0.5439	0.2943	0.0702
DC	−1.4701	0.0743	0.1898	−4.2006	4.5621×10^{-5}**	0.5423	−0.7661	0.2233	0.0989
VMHC Δ	−8.6851	1.9192×10^{-12}**	1.1212				−0.7894	0.2165	0.1019

	Robust paired *t*-test within normal controls			Robust Independent *t*-test between patients and normal controls					
	With *Z*-Standardization			Without *Z*-Standardization			With *Z*-Standardization		
	t	*p*	*ES*	*t*	*p*	*ES*	*t*	*p*	*ES*
ALFF	0.8955	0.8129	0.1156	−1.9403	0.0286*	0.3572	−2.3220	0.0119*	0.4275
fALFF	−0.1923	0.4241	0.0248	−0.5934	0.2776	0.1093	2.0663	0.0205*	0.3804
ReHo	−1.0020	0.1602	0.1294	−0.1415	0.4440	0.0261	1.4652	0.0728	0.2698
DC	−1.1546	0.1265	0.1491	−1.5768	0.0601	0.2903	−0.2559	0.6005	0.0471
VMHC Δ				−6.0005	1.108-5×10^{-8}**	1.1048			

ΔVMHC was not processed with Z-standardization but with Fisher's r-to-z transformation, and thus, results of Z-standardization of this metric are not listed. ES stands for effect size measured by Cohen's d. * stands for $p < .05$, ** stands for $p < .0056$, i.e., survived Bonferroni correction.

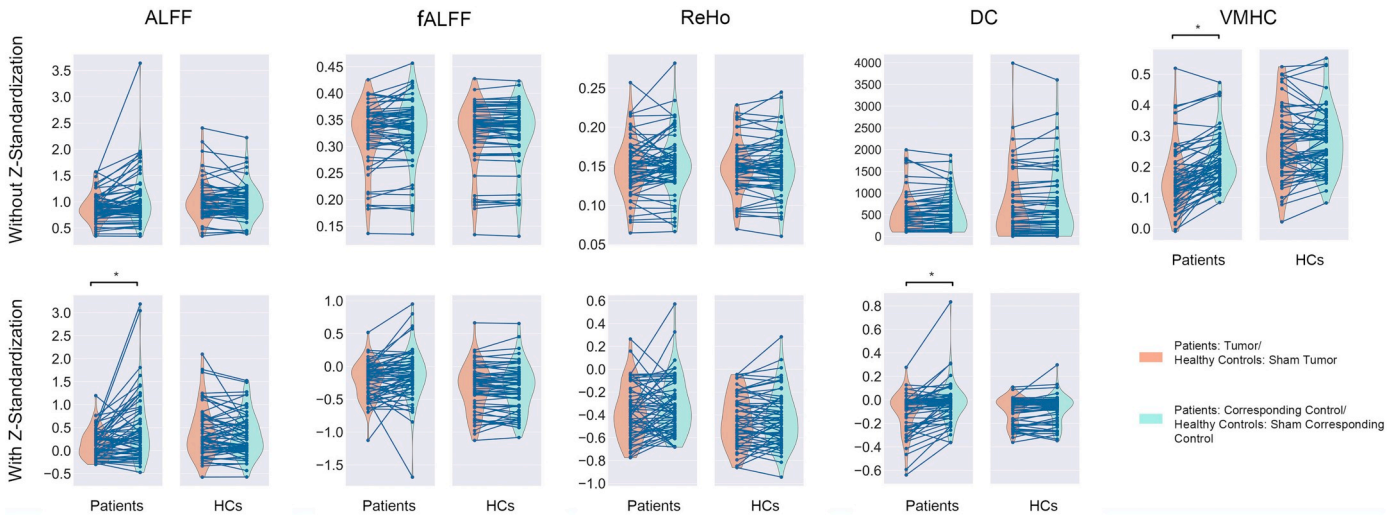

Fig. 2. Common R-fMRI indices of tumors and their corresponding control areas in the patient group and the sham ones in control group. VMHC, which underwent Fisher's r-to-z transformation, could distinguish tumors from corresponding control regions regardless of whether or not Z-standardization was employed (survived Bonferroni correction threshold $p < .05/9 = 0.0056$). Furthermore, ALFF and DC could not differentiate tumors unless employed Z-standardization. However, fALFF and ReHo, which two did not survived Bonferroni correction threshold $p < .0056$, failed to differentiate tumors. (* $p < .0056$).

and presented this analysis in the supplementary materials. DC still could not significantly differentiate tumors significantly, and this persisted even when Z-standardization was employed (Table S1 and Fig. S1). These findings suggest that GSR decreases, not increases, the ability of R-fMRI indices to differentiate tumors. Of note, these investigations did not aim to show R-fMRI indices can be better or additional to conventional tumor imaging biomarkers, but to validate the physiological significance of R-fMRI metrics.

4.1. Utilities of common R-fMRI metrics in differentiating structural lesions

Previous studies have suggested that low-frequency (typically 0.01–0.1 Hz) oscillations (LFO) are related to metabolic correlations of neuronal activity. Researchers have explored the amplitude of BOLD signals in healthy populations and found that ALFF exhibits significant differences among different brain tissues (e.g., GM and WM) (Biswal et al., 1995), different brain regions (e.g., visual and auditory regions) and different physiological states (e.g., eyes closed vs. eyes open) (Yan et al., 2009; Yang et al., 2007). Fractional ALFF (fALFF) approach was defined as the ratio of the low-frequency power spectrum (0.01–0.1 Hz) to the power spectrum of the entire detectable frequency range. As a normalized index of ALFF, fALFF can provide a more specific measure of low-frequency oscillatory phenomena and selectively suppress artifacts from non-specific brain areas, particularly in the perivascular,

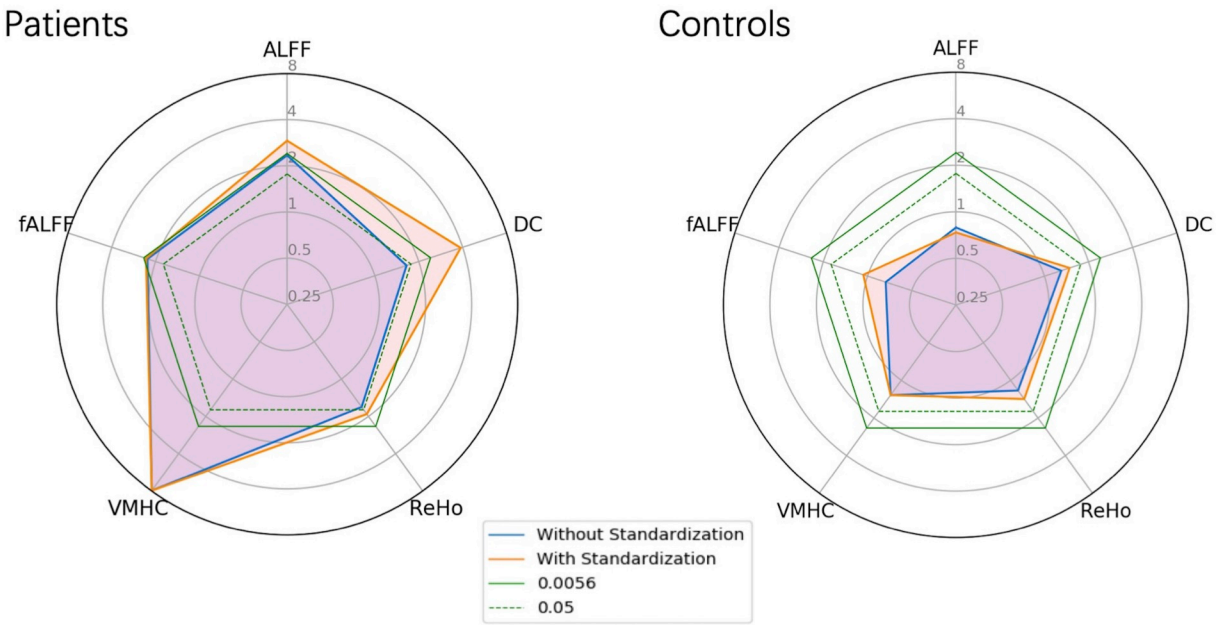

Fig. 3. Different profiles of the five R-fMRI indices in differentiating tumors. VMHC showed the most significant difference, followed by DC (with Z-standardization) and ALFF. Meanwhile, the significance of the five indices in controls were all higher than 0.05, regardless of whether no not Z-standardization was employed. For visualization, the p values were z-transformed. The green lines stand for $p = .0056$ (0.05 after Bonferroni correction), and dashed green lines stand for $p = .05$. The blue line shows Z values of each metric calculated using robust paired t-tests without Z-standardization, and the oranges line indicates the z values of each metric calculated using robust paired t-tests with Z-standardization (For VMHC, Fisher's r-to-z transformation was performed, and its values are shown on the blue and orange lines).

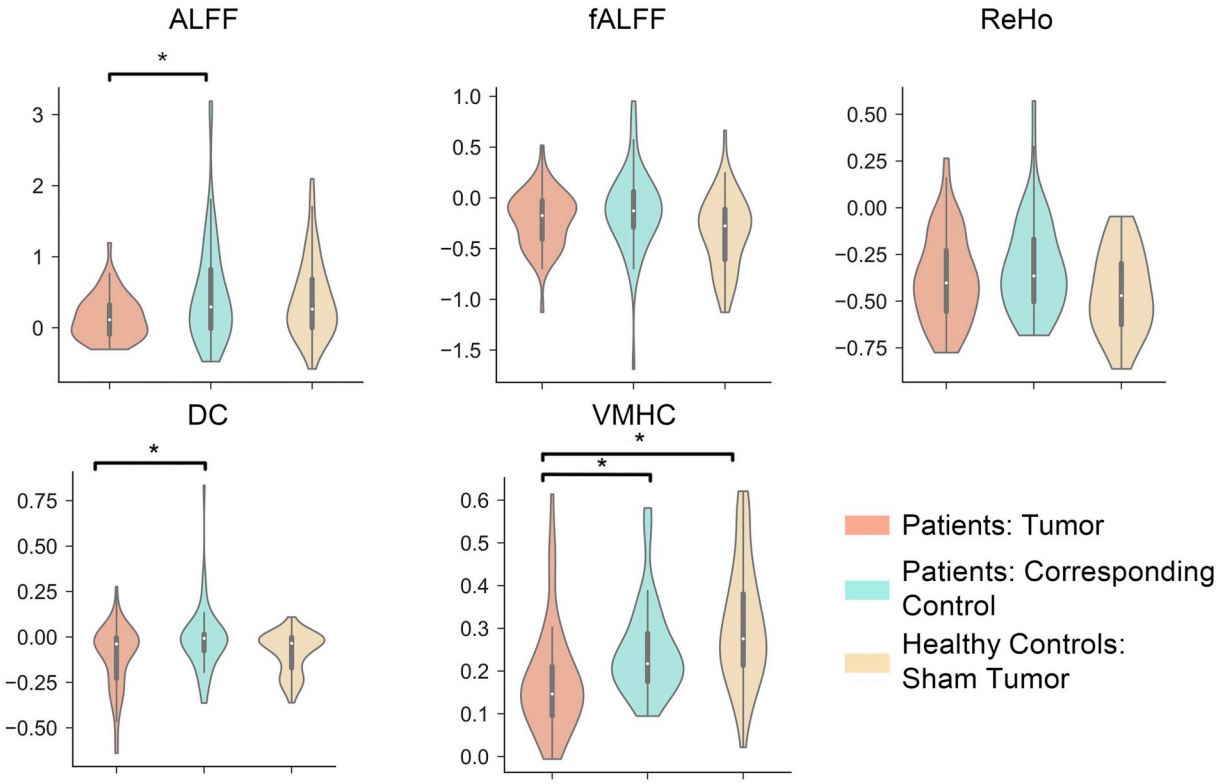

Fig. 4. Common R-fMRI indices of tumors and their corresponding control areas in the patient group and of sham tumors in the healthy control group. We compared each R-fMRI measure of the tumors with those of the sham tumors in the matched controls, assuming that they had the same tumors in the same locations. As the patient tumor and sham tumor came from different subjects, we were able to investigate a between-subject design. Only VMHC succeeded in distinguishing tumors from corresponding control regions (cannot survive Bonferroni correction threshold 0.05/9 = 0.0056). ALFF and DC failed, although they demonstrated significant differences ($p < .0056$) in the within-subject design. In this analysis, all metrics (except for VMHC, which was compared after Fisher's r-to-z transformation) were calculated with Z-standardization, which is critical for R-fMRI metrics, as shown in Fig. 3 (* $p < .0056$).

periventricular and periaqueductal regions (He et al., 2007; Zuo et al., 2010a). Both ALFF and fALFF were used as promising indices to discover biomarker in basal and clinical researches (Han et al., 2011; He et al., 2007; Hou et al., 2014; Qian et al., 2015; Yu et al., 2014; Zang et al., 2007; Zou et al., 2008). When applied to brains with a definitely local pathological structure, both ALFF and fALFF showed lower values within the tumor masks than in the counterpart regions, providing sort of proofs that they were suggestive for regional spontaneous neuronal activity. However, only *Z*-standardized ALFF succeeded in differentiating tumors after applying a stringent correction, suggesting its importance in exploring abnormal activities of diseased brains. That also reminds us again that the group statistical maps for these two measures are similar, but not entirely concordant (Zuo et al., 2010a). For example, previous researches have revealed that different low-frequency bands showed distinct ALFF and fALFF spatial profiles. On the other hand, voxels exhibiting significantly greater ALFF than fALFF were almost located within gray matter (Biswal et al., 1995; Zuo et al., 2010a). All the cases we chose in this study were cerebellar tumors and the convolutions of cerebellar gray matter were sufficiently more complex, which may lead to the different organization of network. Meanwhile, these tumors could cause different space occupying effect that reduces the space of ambient cistern and causes vascular deformation, that leads to differences between ALFF and fALFF. All these issues above should be considered in interpreting the failure of fALFF, whose ability to differentiate local lesions was significant ($p < .05$) but did not survive the further correction ($p < .0056$). Despite these, it is still recommended to report scientific results with both indices in the future study for their close relationship.

ReHo, which represents the KCC between a given voxel's time-series and its 26 adjacent neighbors, differentiated voxels that were more temporally homogeneous within a functional brain area when the area was involved in a specific condition (Zang et al., 2004). ReHo serves as a data-driven R-fMRI metric for investigating neural activities in normal brain networks and clinical features in several diseases, such as AD (Liu et al., 2008; Zhang et al., 2012), PD (Wu et al., 2009), epilepsy (Zhong et al., 2011) and psychiatric disorders (Dichter et al., 2015; Dutta et al., 2014; Paakki et al., 2010; Peng et al., 2014; Yuan et al., 2008), and it reflects stable trait properties with excellent test-retest reliability (Jiang and Zuo, 2016; Zuo et al., 2013). Although as a robust R-fMRI metric (Zuo and Xing, 2014), ReHo failed to differentiate tumors from normal regions. Even employed *Z*-standardization, the differences showed a p value $< .05$ but still cannot survive correction. ReHo represents functional homogeneity of nearby voxels involved in a given region, and voxels in tumor may have similar activities to some extent. Although these voxels do not display fluctuations as normal neural activities do, they have the same blood supplies to shape and couple their sham "functional signals" by hemodynamic response, which causes tumors to mimic the homogeneous sham situation. This result emphasizes the fact again that R-fMRI signals are derived from the hemodynamic reactions and the importance of considering physiological noise in R-fMRI studies.

Extensive evidence suggests that some brain areas act as hubs that are distinctively interconnected distinctively, functionally specialized systems. However, these hubs are susceptible to disconnection and dysfunction in certain brain disorders (Buckner et al., 2009; Zuo et al., 2012). DC is the number or sum of weights of significant connections for a voxel. As such, centrality measures allow us to capture the complexity of the functional networks as a whole. We calculated the weighted sum of positive correlations by requiring each connection's correlation coefficient to exceed a threshold of $r > 0.25$ (Buckner

et al., 2009). Unfortunately, as a global index, DC could not discriminate tumors from corresponding control areas in our unless standardization was employed. One possible explanation is fMRI indices generally showed moderate test-retest reliability in general, but DC showed lower performance than local metrics, ALFF for instance (Wang et al., 2017). This view was consistent with our study. DC as a low test-retest reliability measure was easily affected by a variety of experimental and analytical strategies, such as computational space, GSR and head motion (Zuo and Xing, 2014). GSR even had a substantial influence on its spatial pattern (Liao et al., 2013; Murphy and Fox, 2016). This study highlights the importance of employing *Z*-standardization rather than GSR when exploring functional networks using DC, not only because its test-retest reliability improved without GSR (Liao et al., 2013), but also because DC with Z-standardization had the ability to differentiate structural lesions.

The high degree of synchrony in spontaneous activity between geometrically corresponding inter-hemispheric regions is a fundamental characteristic of the intrinsic functional architecture of the brain. VMHC (Anderson et al., 2011; Zuo et al., 2010b) represents a useful screening method for evaluating homotopic connectivity which is ubiquitous and regionally specific across the whole brain. As a robust index with fair to excellent test-retest reliability (Zuo and Xing, 2014), VMHC is suitable for discovering the underlying physiological mechanisms of normal brain development and aging, as well as the diseased brain. And it has already been applied in studying many pathophysiological disorders, such as autism (Anderson et al., 2011), schizophrenia (Hoptman et al., 2012), seizures (Ji et al., 2014) and AD (Dai et al., 2015). Our study revealed a consistent result that VMHC not only was able to differentiate structural lesions from normal areas, but also turned out to be the most reliable measure with the highest significance level and largest effect size. Although the counterpart normal regions defined differently from other indices, the enrolled subjects had clear boundary tumors, that can mitigate this concern. And the results proved again that VMHC is a credible measure to explore intrinsic network architecture.

4.2. The significance of Z-standardization

Remarkable site-related variations along with a multitude of experimental, environmental and subject-related factors further challenge R-fMRI measures, especially given that R-fMRI research has entered the era of “big data” (Bzdok and Yeo, 2017; Xia and He, 2017; Yan et al., 2013b). Big data from multiple centers play a practical role in clinical applications, particularly holding promise for use in validating biomarkers with the assistance of advanced data-intensive machine learning methodologies, such as deep learning (Arbabshirani et al., 2017). Recently, an intriguing study using R-fMRI data from 1200 subjects offered an impressive example in which subtypes of depression could be defined by R-fMRI data (Drysdale et al., 2017). Another connectome-based study reported the prediction of biomarkers study in autism patients using big data (Abraham et al., 2017). However, with new advances come new challenges. Big data also provides a stark portrayal of variability in imaging methodologies employed in the neuroimaging field (Teipel et al., 2017; Wald and Polimeni, 2017). Big Data can be easily polluted by noise due to the aggregation of data collected via different research designs and data collection methods, particularly imaging sites (Xia and He, 2017), which emphasizes the need to establish consistent acquisition protocols, relevant equipment and software throughout studies. Unfortunately, standardizing all of these factors across studies is not always feasible. Although studies have highlighted the utility of post-acquisition standardization techniques in minimizing the influences of nuisance variables on inter-individual variation (Yan et al., 2013b), less is known regarding the validity of such techniques in lesion differentiation. This research found most indices could differentiate tumors after employing *Z*-standardization, although fALFF and ReHo were not able to pass the correction ($0.0056 < p < .05$). Moreover, ALFF and DC failed to differentiate tumors unless Z-standardization was performed. Employing Z-standardization was effective in reducing nuisance effects and increasing test-retest reliability, allowing ALFF and DC to succeed in differentiating tumors even performed rigid correction. As a post-hoc standardization strategy was used widely, this study offers a new understanding of the substantial necessity of Z-standardization in the era of big data.

4.3. Within-subject designs are crucial for R-fMRI research

Within-subject designs have gained popularity for their ability to decrease participant-related nuisance variations and increase power. Researchers should generally prefer within-subject designs to between-subject designs when possible, as larger effect sizes in within-subject designs can increase reproducibility in small-sample-size studies (Chen et al., 2018; Mumford et al., 2014). This study emphasized the importance of within-subject designs again, as some R-fMRI indices, ALFF and DC, for instance, could not differentiate tumors when calculated using the between-subject design, which compared the R-fMRI metrics of tumors with sham tumors in controls using the robust two-sample *t*-test, even after employing Z-standardization. This result is in contrast to the within-subject design, for which more R-fMRI indices (ALFF and DC pass the correction, fALFF and ReHo did not pass the correction) were able to distinguish tumors from normal brain regions with Z-standardization. Therefore, researchers should prioritize within-subject designs over between-subject designs whenever possible.

4.4. Limitations and future directions

This study is characterized by several limitations. First, we only used cerebellar tumors to test the validity if R-fMRI indices in differentiating lesions. This is because cerebellar asymmetry is weaker than cerebral asymmetry from a structural (Ito, 1984) and functional perspective (Wang et al., 2013). Furthermore, the cerebellum contains nearly 4 times more neurons than the cerebral cortex but has a much smaller volume, and thus, cerebellar tumors caused less anatomic distortions in spatial normalization (Agarwal et al., 2017). Second, we only explored the differences in R-fMRI metrics between tumors and normal areas, but we did not compare their performances with other multi-modal MRI sequences. We plan to study the relations between R-fMRI and perfusion MRI (cerebral blood flow), for different vascularity of tumors could serve as a potential reason for the changes in ALFF/fALFF. Third, although > 80 subjects (40 per group) were recommended for fMRI research for reliability and sensitivity and our sample size were enough (Chen et al., 2018), a much larger sample size would give us the opportunity to study on different tumor pathological types, such as hypervascular tumors and hypovascular tumors, solid tumors and cystic tumors, which may provide new insight into physiological significance of R-fMRI signals and artifacts. These limitations summarize additional aspects that we plan to explore in the future.

5. Conclusions

To the best of our knowledge, this is the first study to comprehensively evaluate the ability of different R-fMRI metrics to differentiate structural lesions, which should be the premise of identifying R-fMRI biomarkers in neuropsychiatric disorders or mapping eloquent areas and epileptic foci. VMHC were able to discriminate tumors from normal regions, while ALFF and DC failed to differentiate structural lesions (brain tumors) unless Z-standardization was employed. These results validated the implicit assumptions from the perspective of neurosurgeon that R-fMRI signals represented neural activity rather than noise. Furthermore, we recommend within-subject designs over between-subject designs whenever possible.

Conflict of interest

The authors declare no competing financial interests.

Acknowledgements

The authors thank the reviewers for their careful work and constructive comments, Zhong Yang for assembling the image database. This work was supported by the Natural Science Foundation and Major Basic Research Program of Shanghai (16JC1420100); “Shuguang Program” of Shanghai Education Development Foundation and Shanghai Municipal Education Commission (16SG02); Shanghai Municipal Science and Technology Major Project (2018SHZDZX01); Shanghai Municipal Health Commission Intelligence Medical Program (2018ZHYL0107); Shanghai Municipal Health Commission Subject Chief Scientist (2018); National Key R&D Program of China (2017YFC1309902); The National Natural Science Foundation of China (81671774 and 81630031); the Hundred Talents Program and the 13th Five-year Informatization Plan (XXH13505) of Chinese Academy of Sciences; Beijing Municipal Science & Technology Commission (Z161100000216152).

Appendix A. Supplementary data

Supplementary data to this article can be found online at https://doi.org/10.1016/j.nicl.2019.101741.

References

Abraham, A., Milham, M.P., Di Martino, A., Craddock, R.C., Samaras, D., Thirion, B., Varoquaux, G., 2017. Deriving reproducible biomarkers from multi-site resting-state data: An autism-based example. Neuroimage 147, 736–745.

Agarwal, S., Sair, H.I., Pillai, J.J., 2017. Limitations of resting-state functional MR imaging in the setting of focal brain lesions. Neuroimaging Clin. N. Am. 27, 645–661.

Anderson, J.S., Druzgal, T.J., Froehlich, A., DuBray, M.B., Lange, N., Alexander, A.L., Abildskov, T., Nielsen, J.A., Cariello, A.N., Cooperrider, J.R., Bigler, E.D., Lainhart, J.E., 2011. Decreased interhemispheric functional connectivity in autism. Cereb. Cortex 21, 1134–1146.

Arbabshirani, M.R., Plis, S., Sui, J., Calhoun, V.D., 2017. Single subject prediction of brain disorders in neuroimaging: promises and pitfalls. Neuroimage 145, 137–165.

Ashburner, J., 2007. A fast diffeomorphic image registration algorithm. Neuroimage 38, 95–113.

Ashburner, J., Friston, K.J., 2005. Unified segmentation. Neuroimage 26, 839–851.

Baria, A.T., Baliki, M.N., Parrish, T., Apkarian, A.V., 2011. Anatomical and functional assemblies of brain BOLD oscillations. J. Neurosci. 31, 7910–7919.

Biswal, B., Zerrin Yetkin, F., Haughton, V.M., Hyde, J.S., 1995. Functional connectivity in the motor cortex of resting human brain using echo-planar mri. Magn. Reson. Med. 34, 537–541.

Biswal, B.B., Mennes, M., Zuo, X.-N., Gohel, S., Kelly, C., Smith, S.M., Beckmann, C.F., Adelstein, J.S., Buckner, R.L., Colcombe, S., Dogonowski, A.-M., Ernst, M., Fair, D., Hampson, M., Hoptman, M.J., Hyde, J.S., Kiviniemi, V.J., Kötter, R., Li, S.-J., Lin, C.-P., Lowe, M.J., Mackay, C., Madden, D.J., Madsen, K.H., Margulies, D.S., Mayberg, H.S., McMahon, K., Monk, C.S., Mostofsky, S.H., Nagel, B.J., Pekar, J.J., Peltier, S.J., Petersen, S.E., Riedl, V., Rombouts, S.A.R.B., Rypma, B., Schlaggar, B.L., Schmidt, S., Seidler, R.D., Siegle, G.J., Sorg, C., Teng, G.-J., Veijola, J., Villringer, A., Walter, M., Wang, L., Weng, X.-C., Whitfield-Gabrieli, S., Williamson, P., Windischberger, C., Zang, Y.-F., Zhang, H.-Y., Castellanos, F.X., Milham, M.P., 2010. Toward discovery science of human brain function. Proc. Natl. Acad. Sci. 107, 4734–4739.

Buckner, R.L., Sepulcre, J., Talukdar, T., Krienen, F.M., Liu, H., Hedden, T., Andrews-Hanna, J.R., Sperling, R.A., Johnson, K.A., 2009. Cortical hubs revealed by intrinsic functional connectivity: mapping, assessment of stability, and relation to Alzheimer's disease. J. Neurosci. 29, 1860–1873.

Bzdok, D., Yeo, B.T.T., 2017. Inference in the age of big data: future perspectives on neuroscience. Neuroimage 155, 549–564.

Castellanos, F.X., Di Martino, A., Craddock, R.C., Mehta, A.D., Milham, M.P., 2013. Clinical applications of the functional connectome. Neuroimage 80, 527–540.

Caulfield, M.D., Zhu, D.C., McAuley, J.D., Servatius, R.J., 2016. Individual differences in resting-state functional connectivity with the executive network: support for a cerebellar role in anxiety vulnerability. Brain Struct. Funct. 221, 3081–3093.

Chen, X., Lu, B., Yan, C.-G., 2018. Reproducibility of R-fMRI metrics on the impact of different strategies for multiple comparison correction and sample sizes. Hum. Brain Mapp. 39, 300–318.

Craddock, R.C., Jbabdi, S., Yan, C.-G., Vogelstein, J.T., Castellanos, F.X., Di Martino, A., Kelly, C., Heberlein, K., Colcombe, S., Milham, M.P., 2013. Imaging human connectomes at the macroscale. Nat. Methods 10, 524.

Dai, Z., Yan, C., Li, K., Wang, Z., Wang, J., Cao, M., Lin, Q., Shu, N., Xia, M., Bi, Y., He, Y., 2015. Identifying and mapping connectivity patterns of brain network hubs in Alzheimer's disease. Cereb. Cortex 25, 3723–3742.

Di Martino, A., Yan, C.G., Li, Q., Denio, E., Castellanos, F.X., Alaerts, K., Anderson, J.S., Assaf, M., Bookheimer, S.Y., Dapretto, M., Deen, B., Delmonte, S., Dinstein, I., Ertl-Wagner, B., Fair, D.A., Gallagher, L., Kennedy, D.P., Keown, C.L., Keysers, C., Lainhart, J.E., Lord, C., Luna, B., Menon, V., Minshew, N.J., Monk, C.S., Mueller, S., Muller, R.A., Nebel, M.B., Nigg, J.T., O'Hearn, K., Pelphrey, K.A., Peltier, S.J., Rudie, J.D., Sunaert, S., Thioux, M., Tyszka, J.M., Uddin, L.Q., Verhoeven, J.S., Wenderoth, N., Wiggins, J.L., Mostofsky, S.H., Milham, M.P., 2014. The autism brain imaging data exchange: towards a large-scale evaluation of the intrinsic brain architecture in autism. Mol. Psychiatry 19, 659–667.

Dichter, G.S., Gibbs, D., Smoski, M.J., 2015. A systematic review of relations between resting-state functional-MRI and treatment response in major depressive disorder. J. Affect. Disord. 172, 8–17.

Drysdale, A.T., Grosenick, L., Downar, J., Dunlop, K., Mansouri, F., Meng, Y., Fetcho, R.N., Zebley, B., Oathes, D.J., Etkin, A., Schatzberg, A.F., Sudheimer, K., Keller, J., Mayberg, H.S., Gunning, F.M., Alexopoulos, G.S., Fox, M.D., Pascual-Leone, A., Voss, H.U., Casey, B.J., Dubin, M.J., Liston, C., 2017. Resting-state connectivity biomarkers define neurophysiological subtypes of depression. Nat. Med. 23, 28–38.

Dumouchel, W., O'Brien, F., 1992. Integrating a robust option into a multiple regression computing environment. In: Computing and Graphics in Statistics. Springer-Verlag New York, Inc., pp. 41–48.

Dutta, A., McKie, S., Deakin, J.F.W., 2014. Resting state networks in major depressive disorder. Psychiatry Res. Neuroimaging 224, 139–151.

Eklund, A., Nichols, T.E., Knutsson, H., 2016. Cluster failure: why fMRI inferences for spatial extent have inflated false-positive rates. Proc. Natl. Acad. Sci. 113, 7900–7905.

Friston, K.J., Williams, S., Howard, R., Frackowiak, R.S.J., Turner, R., 1996. Movement-related effects in fMRI time-series. Magn. Reson. Med. 35, 346–355.

Hacker, C.D., Snyder, A.Z., Pahwa, M., Corbetta, M., Leuthardt, E.C., 2017. Frequency-specific electrophysiologic correlates of resting state fMRI networks. Neuroimage 149, 446–457.

Han, Y., Wang, J., Zhao, Z., Min, B., Lu, J., Li, K., He, Y., Jia, J., 2011. Frequency-dependent changes in the amplitude of low-frequency fluctuations in amnestic mild cognitive impairment: a resting-state fMRI study. Neuroimage 55, 287–295.

He, Y., Wang, L., Zang, Y., Tian, L., Zhang, X., Li, K., Jiang, T., 2007. Regional coherence changes in the early stages of Alzheimer's disease: a combined structural and resting-state functional MRI study. Neuroimage 35, 488–500.

He, B.J., Snyder, A.Z., Zempel, J.M., Smyth, M.D., Raichle, M.E., 2008. Electrophysiological correlates of the brain's intrinsic large-scale functional architecture. Proc. Natl. Acad. Sci. 105, 16039–16044.

Hoptman, M.J., Zuo, X.N., D'Angelo, D., Mauro, C.J., Butler, P.D., Milham, M.P., Javitt, D.C., 2012. Decreased interhemispheric coordination in schizophrenia: a resting state fMRI study. Schizophr. Res. 141, 1–7.

Hou, Y., Wu, X., Hallett, M., Chan, P., Wu, T., 2014. Frequency-dependent neural activity in Parkinson's disease. Hum. Brain Mapp. 35, 5815–5833.

Ito, M., 1984. The Cerebellum and Neural. Control.

Ji, G.-J., Zhang, Z., Xu, Q., Zang, Y.-F., Liao, W., Lu, G., 2014. Generalized tonic-Clonic seizures: aberrant Interhemispheric functional and anatomical connectivity. Radiology 271, 839–847.

Jiang, L., Zuo, X.N., 2016. Regional homogeneity: a multimodal, multiscale neuroimaging marker of the human Connectome. Neuroscientist 22, 486–505.

Jiang, Z., Krainik, A., David, O., Salon, C., Troprès, I., Hoffmann, D., Pannetier, N., Barbier, E.L., Bombìn, E.R., Warnking, J., Pasteris, C., Chabardes, S., Berger, F., Grand, S., Segebarth, C., Gay, E., Le Bas, J.-F., 2010. Impaired fMRI activation in patients with primary brain tumors. Neuroimage 52, 538–548.

Kapur, S., Phillips, A.G., Insel, T.R., 2012. Why has it taken so long for biological psychiatry to develop clinical tests and what to do about it? Mol. Psychiatry 17, 1174–1179.

Keller, C.J., Bickel, S., Entz, L., Ulbert, I., Milham, M.P., Kelly, C., Mehta, A.D., 2011. Intrinsic functional architecture predicts electrically evoked responses in the human brain. Proc. Natl. Acad. Sci. 108, 10308–10313.

Kelly, C., Uddin, L.Q., Shehzad, Z., Margulies, D.S., Castellanos, F.X., Milham, M.P., Petrides, M., 2010. Broca's region: linking human brain functional connectivity data and non-human primate tracing anatomy studies. Eur. J. Neurosci. 32, 383–398.

Lang, S., Duncan, N., Northoff, G., 2014. Resting-state functional magnetic resonance imaging: review of neurosurgical applications. Neurosurgery 74, 453–464 (discussion 464-455).

Leopold, D.A., Maier, A., 2012. Ongoing physiological processes in the cerebral cortex. Neuroimage 62, 2190–2200.

Liao, X.H., Xia, M.R., Xu, T., Dai, Z.J., Cao, X.Y., Niu, H.J., Zuo, X.N., Zang, Y.F., He, Y., 2013. Functional brain hubs and their test-retest reliability: a multiband resting-state functional MRI study. Neuroimage 83, 969–982.

Liu, T.T., 2013. Neurovascular factors in resting-state functional MRI. Neuroimage 80, 339–348.

Liu, Y., Wang, K., Yu, C., He, Y., Zhou, Y., Liang, M., Wang, L., Jiang, T., 2008. Regional homogeneity, functional connectivity and imaging markers of Alzheimer's disease: a review of resting-state fMRI studies. Neuropsychologia 46, 1648–1656.

Liu, X., Zhu, X.H., Zhang, Y., Chen, W., 2011. Neural origin of spontaneous hemodynamic fluctuations in rats under burst-suppression anesthesia condition. Cereb. Cortex 21, 374–384.

Margulies, D.S., Vincent, J.L., Kelly, C., Lohmann, G., Uddin, L.Q., Biswal, B.B., Villringer, A., Castellanos, F.X., Milham, M.P., Petrides, M., 2009. Precuneus shares intrinsic functional architecture in humans and monkeys. Proc. Natl. Acad. Sci. 106, 20069–20074.

Mumford, J.A., Davis, T., Poldrack, R.A., 2014. The impact of study design on pattern estimation for single-trial multivariate pattern analysis. Neuroimage 103, 130–138.

Murphy, K., Fox, M.D., 2016. Towards a consensus regarding global signal regression for resting state functional connectivity MRI. Neuroimage. 154, 169–173.
Nostro, A.D., Müller, V.I., Varikuti, D.P., Pläschke, R.N., Hoffstaedter, F., Langner, R., Patil, K.R., Eickhoff, S.B., 2018. Predicting personality from network-based resting-state functional connectivity. Brain Struct. Funct. 223, 2699–2719.
Paakki, J.-J., Rahko, J., Long, X., Moilanen, I., Tervonen, O., Nikkinen, J., Starck, T., Remes, J., Hurtig, T., Haapsamo, H., Jussila, K., Kuusikko-Gauffin, S., Mattila, M.-L., Zang, Y., Kiviniemi, V., 2010. Alterations in regional homogeneity of resting-state brain activity in autism spectrum disorders. Brain Res. 1321, 169–179.
Peng, D.-C., Dai, X.-J., Gong, H.-H., Li, H.-J., Nie, X., Zhang, W., 2014. Altered intrinsic regional brain activity in male patients with severe obstructive sleep apnea: a resting-state functional magnetic resonance imaging study. Neuropsychiatr. Dis. Treat. 10, 1819–1826.
Pernet, C.R., Wilcox, R., Rousselet, G.A., 2012. Robust correlation analyses: false positive and power validation using a new open source matlab toolbox. Front. Psychol. 3, 606.
Pernet, C.R., Gorgolewski, K.J., Job, D., Rodriguez, D., Whittle, I., Wardlaw, J., 2016. A structural and functional magnetic resonance imaging dataset of brain tumour patients. Sci Data 3, 160003.
Power, Jonathan D., Schlaggar, Bradley L., Petersen, Steven E., 2014. Studying brain organization via spontaneous fMRI signal. Neuron 84, 681–696.
Qian, L., Zhang, Y., Zheng, L., Shang, Y., Gao, J.H., Liu, Y., 2015. Frequency dependent topological patterns of resting-state brain networks. PLoS One 10, e0124681.
Qiu, T.M., Yan, C.G., Tang, W.J., Wu, J.S., Zhuang, D.X., Yao, C.J., Lu, J.F., Zhu, F.P., Mao, Y., Zhou, L.F., 2014. Localizing hand motor area using resting-state fMRI: validated with direct cortical stimulation. Acta Neurochir. 156, 2295–2302.
Rousselet, G.A., Foxe, J.J., Bolam, J.P., 2016. A few simple steps to improve the description of group results in neuroscience. Eur. J. Neurosci. 44, 2647–2651.
Satterthwaite, T.D., Elliott, M.A., Gerraty, R.T., Ruparel, K., Loughead, J., Calkins, M.E., Eickhoff, S.B., Hakonarson, H., Gur, R.C., Gur, R.E., Wolf, D.H., 2013. An improved framework for confound regression and filtering for control of motion artifact in the preprocessing of resting-state functional connectivity data. Neuroimage 64, 240–256.
Scholvinck, M.L., Leopold, D.A., Brookes, M.J., Khader, P.H., 2013. The contribution of electrophysiology to functional connectivity mapping. Neuroimage 80, 297–306.
Teipel, S.J., Wohlert, A., Metzger, C., Grimmer, T., Sorg, C., Ewers, M., Meisenzahl, E., Kloppel, S., Borchardt, V., Grothe, M.J., Walter, M., Dyrba, M., 2017. Multicenter stability of resting state fMRI in the detection of Alzheimer's disease and amnestic MCI. Neuroimage Clin 14, 183–194.
Wald, L.L., Polimeni, J.R., 2017. Impacting the effect of fMRI noise through hardware and acquisition choices - implications for controlling false positive rates. Neuroimage 154, 15–22.
Wang, D., Buckner, R.L., Liu, H., 2013. Cerebellar asymmetry and its relation to cerebral asymmetry estimated by intrinsic functional connectivity. J. Neurophysiol. 109, 46–57.
Wang, J., Ren, Y., Hu, X., Nguyen, V.T., Guo, L., Han, J., Guo, C.C., 2017. Test-retest reliability of functional connectivity networks during naturalistic fMRI paradigms. Hum. Brain Mapp. 38, 2226–2241.
Weissgerber, T.L., Milic, N.M., Winham, S.J., Garovic, V.D., 2015. Beyond bar and line graphs: time for a new data presentation paradigm. PLoS Biol. 13, e1002128.
Wilcox, R.R., Rousselet, G.A., 2018. A guide to robust statistical methods in neuroscience. Curr Protoc Neurosci 82, 8.42.41–48.42.30.
Wu, T., Long, X., Zang, Y., Wang, L., Hallett, M., Li, K., Chan, P., 2009. Regional homogeneity changes in patients with Parkinson's disease. Hum. Brain Mapp. 30, 1502–1510.
Xia, M., He, Y., 2017. Functional connectomics from a "big data" perspective. Neuroimage. 160, 152–167.
Yan, C.G., Zang, Y.F., 2010. DPARSF: a MATLAB toolbox for "pipeline" data analysis of resting-state fMRI. Front. Syst. Neurosci. 4, 13.
Yan, C., Liu, D., He, Y., Zou, Q., Zhu, C., Zuo, X., Long, X., Zang, Y., 2009. Spontaneous brain activity in the default mode network is sensitive to different resting-state conditions with limited cognitive load. PLoS One 4, e5743.
Yan, C.-G., Cheung, B., Kelly, C., Colcombe, S., Craddock, R.C., Di Martino, A., Li, Q., Zuo, X.-N., Castellanos, F.X., Milham, M.P., 2013a. A comprehensive assessment of regional variation in the impact of head micromovements on functional connectomics. Neuroimage 76, 183–201.
Yan, C.G., Craddock, R.C., Zuo, X.N., Zang, Y.F., Milham, M.P., 2013b. Standardizing the intrinsic brain: towards robust measurement of inter-individual variation in 1000 functional connectomes. Neuroimage 80, 246–262.
Yan, C.G., Wang, X.D., Zuo, X.N., Zang, Y.F., 2016. DPABI: Data Processing & Analysis for (resting-state) brain imaging. Neuroinformatics 14, 339–351.
Yang, H., Long, X.Y., Yang, Y., Yan, H., Zhu, C.Z., Zhou, X.P., Zang, Y.F., Gong, Q.Y., 2007. Amplitude of low frequency fluctuation within visual areas revealed by resting-state functional MRI. Neuroimage 36, 144–152.
Yu, R., Chien, Y.L., Wang, H.L., Liu, C.M., Liu, C.C., Hwang, T.J., Hsieh, M.H., Hwu, H.G., Tseng, W.Y., 2014. Frequency-specific alternations in the amplitude of low-frequency fluctuations in schizophrenia. Hum. Brain Mapp. 35, 627–637.
Yuan, Y., Zhang, Z., Bai, F., Yu, H., Shi, Y., Qian, Y., Liu, W., You, J., Zhang, X., Liu, Z., 2008. Abnormal neural activity in the patients with remitted geriatric depression: a resting-state functional magnetic resonance imaging study. J. Affect. Disord. 111, 145–152.
Zang, Y., Jiang, T., Lu, Y., He, Y., Tian, L., 2004. Regional homogeneity approach to fMRI data analysis. Neuroimage 22, 394–400.
Zang, Y.F., He, Y., Zhu, C.Z., Cao, Q.J., Sui, M.Q., Liang, M., Tian, L.X., Jiang, T.Z., Wang, Y.F., 2007. Altered baseline brain activity in children with ADHD revealed by resting-state functional MRI. Brain and Development 29, 83–91.
Zhang, D., Raichle, M.E., 2010. Disease and the brain's dark energy. Nat. Rev. Neurol. 6, 15–28.
Zhang, Z., Liu, Y., Jiang, T., Zhou, B., An, N., Dai, H., Wang, P., Niu, Y., Wang, L., Zhang, X., 2012. Altered spontaneous activity in Alzheimer's disease and mild cognitive impairment revealed by regional homogeneity. Neuroimage 59, 1429–1440.
Zhong, Y., Lu, G., Zhang, Z., Jiao, Q., Li, K., Liu, Y., 2011. Altered regional synchronization in epileptic patients with generalized tonic–clonic seizures. Epilepsy Res. 97, 83–91.
Zou, Q.H., Zhu, C.Z., Yang, Y., Zuo, X.N., Long, X.Y., Cao, Q.J., Wang, Y.F., Zang, Y.F., 2008. An improved approach to detection of amplitude of low-frequency fluctuation (ALFF) for resting-state fMRI: fractional ALFF. J. Neurosci. Methods 172, 137–141.
Zuo, X.-N., Xing, X.-X., 2014. Test-retest reliabilities of resting-state FMRI measurements in human brain functional connectomics: a systems neuroscience perspective. Neurosci. Biobehav. Rev. 45, 100–118.
Zuo, X.N., Di Martino, A., Kelly, C., Shehzad, Z.E., Gee, D.G., Klein, D.F., Castellanos, F.X., Biswal, B.B., Milham, M.P., 2010a. The oscillating brain: complex and reliable. Neuroimage 49, 1432–1445.
Zuo, X.N., Kelly, C., Di Martino, A., Mennes, M., Margulies, D.S., Bangaru, S., Grzadzinski, R., Evans, A.C., Zang, Y.F., Castellanos, F.X., Milham, M.P., 2010b. Growing together and growing apart: regional and sex differences in the lifespan developmental trajectories of functional homotopy. J. Neurosci. 30, 15034–15043.
Zuo, X.N., Ehmke, R., Mennes, M., Imperati, D., Castellanos, F.X., Sporns, O., Milham, M.P., 2012. Network centrality in the human functional Connectome. Cereb. Cortex 22, 1862–1875.
Zuo, X.N., Xu, T., Jiang, L., Yang, Z., Cao, X.Y., He, Y., Zang, Y.F., Castellanos, F.X., Milham, M.P., 2013. Toward reliable characterization of functional homogeneity in the human brain: preprocessing, scan duration, imaging resolution and computational space. Neuroimage 65, 374–386.